

Design and Experimental Validation of a Computational Effective Dynamic Thermal Energy Storage Tank Model

J. Bonilla^{a,b,*}, M.-M. Rodríguez-García^a, L. Roca^{a,b}, Alberto de la Calle^c,
L.Valenzuela^a

^a*CIEMAT-PSA, Centro de Investigaciones Energéticas, Medioambientales y Tecnológicas -
Plataforma Solar de Almería, Spain*

^b*CIESOL, Solar Energy Research Center, Joint Institute University of Almería - CIEMAT,
Almería, Spain*

^c*CSIRO Energy, 10 Murray Dwyer Ct, Mayfield West, NSW 2304, Australia*

Abstract

Concentrating solar thermal power plants rely in thermal energy storage systems in order to provide a stable power supply. However, they might not been able to meet power plant demands, mainly because of their storage sizes which are restricted due to economic reasons. One way of mitigating this effect is to control in an optimal way the charging and discharging processes. For the design and validation of advanced control strategies, an accurate dynamic model is essential. For this reason, a dynamic thermal energy tank model intended to be used in concentrating solar thermal power plant models is presented in this paper. The developed tank model is validated in charging and discharging processes and also at rest state in order to validate thermal losses dynamics. Simulation results are compared against experimental data from the CIEMAT-PSA molten salt testing facility.

Keywords: Thermal energy storage, sensible heat, dynamic modeling, transient simulation, molten salt, Modelica.

1. Introduction

Dispatchability on demand is the keystone to provide electricity in a stable and reliable way, and one of the main issues that renewable energies must tackle. Solar thermal power has the advantage, over other renewable energies, of storing thermal energy and thus the ability of mitigating solar irradiance variability to some extent [35]. This advantage makes solar thermal power appropriate for large-scale energy production.

*Corresponding author. Tel.: +34 95038780 Ext. 908. E-mail: javier.bonilla@psa.es

Concentrating Solar Power (CSP) technology uses mirrors to concentrate the incoming direct normal irradiance onto a receiver where a working fluid receives heat and thus increases its thermal energy. Thermal energy is used in a thermodynamic cycle to produce electricity. Part of the working fluid thermal energy can be stored heating up a storage fluid which is collected in a Thermal Energy Storage (TES) system. The thermal energy in the storage fluid can be released when needed to produce electricity.

TES systems, however, may not be able to meet the power plant demand, mainly because of their storage sizes which are restricted due to economic reasons. This issue is presently an active research area where hybridization with fossil fuels, as well as with other renewable energy sources, is playing an important role [14]. Another way of improving the plant efficiency is by optimizing the charging and discharging control strategies which highly influence the overall system performance [41]. In this context, accurate dynamic heat exchanger and tank models are important for the design, testing and validation of advanced control strategies.

Different kinds of technologies regarding TES systems: sensible heat, latent heat, thermochemical, have been studied over the years. Nowadays, sensible heat materials (i.e. thermal oil, molten salt) are the most widely used in commercial CSP plants [15].

Tank modeling in the literature is too extensive to be summarized in just one section, due to its relevance in many areas of science and engineering. However, a few of the most recent and relevant works considering process modeling of molten salt TES systems, are briefly commented. In [19], a steady-state tank model integrated in a Parabolic-Trough (PT) solar thermal power plant for performance evaluation is presented, simulation results are validated against experimental data from the Andasol-II power plant. The dynamic model of a PT solar thermal power plant with a direct active two-tank system is introduced in [28], simulation results as well as control techniques are presented in this paper. Dynamic simulation of a CSP plant with a direct two-tank TES are presented in [20]. A model was developed to study how a molten salt TES system could increase the flexibility of a fossil fuel power plant in [21]. In [32], a modular object-oriented approach to model molten salt storage tanks for concentrating solar thermal power plants with focus on transient thermal and fluid dynamic simulations is detailed. An object-oriented dynamic tank model developed in Modelica is presented in [41], heat loss mechanisms are evaluated in such a way than only the most relevant can be considered. Simulation results are shown for charging and discharging processes. In [23], heat losses and tank temperature drop are validated against experimental data, a dynamic tank model developed in Simulink integrated in thermal plants is introduced. This model properly estimates delays and thermal transition behavior, simulation results are validated against experimental data. The performance of CSP oil-cooled plants, with and without molten salt TES systems, was studied in [11]. In [9], the performance of medium size CSP plants based on an Organic Rankine Cycle (ORC) power generation unit with direct two-tank and thermocline TES systems are compared in simulation. Dynamic simulations of a two-tank

indirect molten salt TES lumped parameter model in charging and discharging processes, considering disturbances, are presented in [17]. Transient response simulations of a passive sensible TES system compared to a conventional active indirect two-tank TES unit are studied in [42].

The present paper introduces a dynamic tank model validated against experimental data in terms of heat losses, molten salt and gas temperatures for charging and discharging processes, intended to be used for the improvement of control strategies [30] together with other elements, such as the heat exchanger model [5, 4], that could lead to performance improvements in concentrating solar thermal power plants. The structure of the paper is as follows. The tank, as well as the facility where it belongs, is introduced in Sec. 1.1. Sec. 2 deals with the tank model. Sec. 3 presents simulations, together with the calibration and validation of the tank model. An open source simulation tool to reproduce the obtained results is also introduced. Finally, Sec. 4 draws the main conclusions and future work.

1.1. System Description

A multipurpose molten salt testing facility, with the goal of studying TES system, was set up at Plataforma Solar de Almería (PSA), division of CIEMAT, the public research center for energy, environmental and technological research, which is owned by the Spanish government. The CIEMAT-PSA molten salt testing facility can evaluate and control the heat exchange between molten salts and potential heat transfer fluid for solar thermal power plants, i.e. thermal oil and pressurized gases (air, CO₂, etc.) [34].

The CIEMAT-PSA molten salt testing facility, shown in Fig. 1a, is composed by hot and cold molten salt tanks, a CO₂ - molten salt heat exchanger, a thermal oil loop, two flanged pipe sections and the electrical heat tracing. The thermal oil loop includes the following components: a thermal oil expansion tank, a



(a) General view



(b) Hot molten salt tank

Figure 1: CIEMAT-PSA Molten Salt Testing Facility

Table 1: Tank dimensions, features and parameters

Param.	Description	Value	Units
$c_{p,i}$	Insulation specific heat capacity	840	[39] J/(kg K)
$c_{p,p}$	Pump specific heat capacity	500	¹ J/(kg K)
$c_{p,t}$	Tank wall, floor and roof spec. heat cap.	500	[2] J/(kg K)
$d_{t,in}$	Tank inner diameter	2.5	m
d_p	Pump equivalent diameter	0.186	m
L_b	Inclination base depth	63	mm
L_d	Depth from bottom to level meter	11	mm
L_{pl}	Level meter position relative to center	0.805	m
L_{t1}	Tank height - short side	4.937	m
L_{t2}	Tank height - long side	5.000	m
$L_{tck,t}$	Tank wall, floor and roof thickness	8	mm
$L_{tck,fo}$	Foundation thickness	1.3	m
$L_{tck,i}$	Insulation wall and roof thickness	0.36	m
L_{th12}	Position of thermocouples 1 and 2	0.340	m
L_{th34}	Position of thermocouples 3 and 4	1.570	m
L_{th56}	Position of thermocouples 5 and 6	3.000	m
L_p	Pump length	4.353	m
p_{amb}	Ambient pressure	1	atm
p_t	Tank controlled pressure	50	mbar
k_i	Insulation thermal conductivity	0.240	² W/(m K)
k_{fo}	Foundation thermal conductivity	0.466	² W/(m K)
β_t	Inclination angle	1.432	°
$\rho_{i,ex}$	Insulation density	100	[31] kg/m ³
ρ_p	Pump density	7920	[2] kg/m ³
ρ_w	Tank wall, floor and roof density	7920	¹ kg/m ³
ϵ_l	Liquid emissivity	0.95	³ -
ϵ_p	Pump emissivity	0.305	¹ -
ϵ_t	Tank wall, floor and roof emissivity	0.305	⁴ -

¹ Same values than for the tank metallic structure are assumed.

² Experimentally calibrated value, see Sec. 3.1.

³ Since molten salt is nearly transparent to infrared radiation [36], its mean emissivity value is set to 0.95 [41].

⁴ Emissivity for stainless steel Type 321 is studied in [18]. This paper provides an emissivity estimation value as a function of temperature in the [750 K, 1150 K] range. Assuming that emissivity is wavelength independent and the value provided at the lowest temperature (750 K), the mean emissivity value is fixed to 0.305.

Table 2: Nomenclature

Latin letters					
Var.	Description	Units	Var.	Description	Units
A	Cross-sectional area	m^2	c_p	Spec. heat cap.	$J/(kg\ K)$
C	Heat capacity	J/K	d	Diameter	m
E	Energy	J	E_b	Blackbody power	W/m^2
\dot{E}	Energy flow rate	W	F	View factor	–
G	Incident radiation	W/m^2	Gr	Grashof number	–
h	Spec. enthalpy	J/kg	H	Enthalpy	J
l	Level	m	J	Radiosity	W/m^2
k	Thermal cond.	$W/(m\ K)$	L	Length	m
m	Mass	kg	M	Molar mass	kg/mol
\dot{m}	Mass flow rate	kg/s	Nu	Nusselt number	–
p	Pressure	Pa	P	Perimeter	m
Pr	Prandtl number	–	\dot{Q}	Heat flow rate	W
r	Radius	m	R	Thermal resistance	K/W
Ra	Rayleigh number	–	R_u	Univ. gas const.	$J/(K\ mol)$
S	Surface area	m^2	t	Time	s
T	Temperature	K	u	Spec. int. energy	J/kg
U	Internal energy	J	v	Spec. volume	m^3/kg
V	Volume	m^3	\dot{W}	Power	W
Greek letters					
Var.	Description	Units	Var.	Description	Units
α	Convective coef.	$W/(m^2\ K)$	β	Inclination angle	rad
ϵ	Emissivity	–	ρ	Density	kg/m^3
σ	Stefan-Boltzmann cons.	$W/(m^2\ K^4)$			
Subscripts					
Var.	Description		Var.	Description	
amb	Ambient		b	Base	
c	Characteristic		ch	Channel	
$cond$	Conduction		$conv$	Convection	
cyl	Cylinder		d	Depth	
$disk$	Disk		ex	External	
exp	Experimental		f	Floor	
fo	Foundation		fl	Fluid	
g	Gas		grd	Ground	
i	Insulation		in	Internal	
l	Liquid		$loss$	Loss	
p	Pump		pl	Level meter pos.	
r	Roof		rad	Radiation	
$ring$	Ring		s	Surface	
sim	Simulated		t	Tank	
tck	Thickness		th	Thermocouple	
vp	Vertical plate		w	Wall	

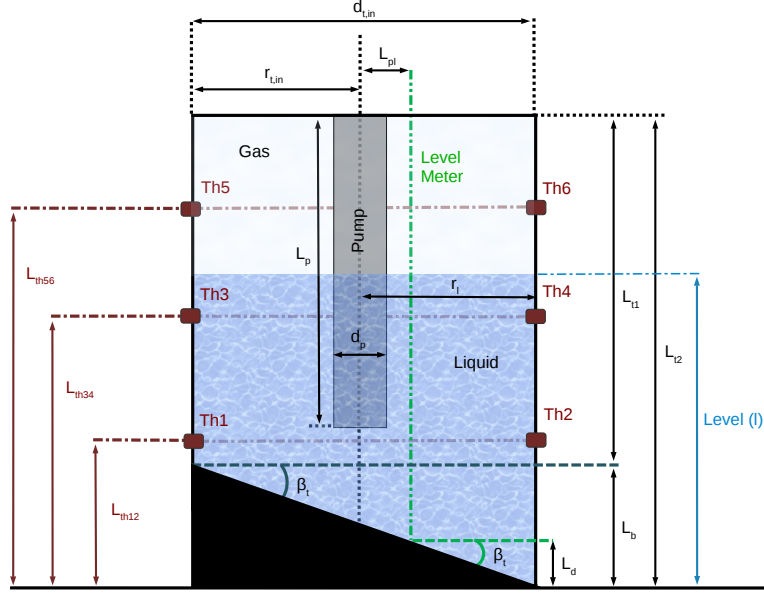


Figure 2: Tank geometry and instrumentation sketch

centrifugal pump, an oil heater, a thermal oil - molten salt heat exchanger, a thermal oil air cooler, an expansion tank and nitrogen bottles to render the molten salt and thermal oil inert. Hot and cold molten salt tanks are in the facility in order to reproduce the sensible-heat thermal storage systems of commercial solar power plants. The cold tank is under ground level. The hot tank is the one considered in this work (see Fig. 1b).

Molten salts can be heated up by means of a thermal oil - molten salt heat exchanger in the thermal oil loop. In turn, thermal oil is heated up by means of an oil heater in the thermal oil loop. This molten salt testing facility is also coupled to the innovative fluids test loop facility by means of a CO_2 - molten salt heat exchanger. This last facility comprises two parabolic-trough collectors and allow studying pressurized gases as heat transfer fluids [33].

Being this facility a reduced scale testing facility of commercial systems and with the aim of being flexible with respect to the tests that can be performed, a diesel oil heater can heat thermal oil up in the thermal oil loop. Then, thermal oil can heat molten salt up by means of a thermal oil - molten salt heat exchanger. Thanks to the oil heater partial loads and transients in the solar field, such as cloud disturbances, can be studied and reproduced.

The cylindrical vertical hot molten salt tank has an inclined base in order to facility its drainage. It is equipped with a level meter, six thermocouples (Th1 to Th6), a vertical pump, thermal insulation, an electrical wall heat tracing system as well as immersed electrical heaters. A sketch of the tank is shown in

Fig. 2, for the sake of clarity the sketch is not at scale, for instance the floor inclination is much lower and the pump is closer to the tank floor. The values of the different distances are listed in Tab. 1, whereas nomenclature is described in Tab. 2.

The tank metallic structure is made of stainless steel, American Society of Mechanical Engineers (ASME) SA240 Type 321, dimensions are given in Tab. 1.

Thermal insulation is built in Rockwool ProRox WM 960. Thickness and mean values for thermal properties, in the facility operation range and according to the manufacturer, are given in Tab. 1. The insulation layer is covered with an aluminum jacket for weather protection.

Molten salt tank foundation designs are commonly outside of standards for foundations, since these standards do not cover the temperature range were TES system operate. Among the most important requirements that this kind of foundations must satisfy are providing good anchorage in order to prevent tank uplift. The foundation must support high temperatures and it must be a good insulator. The hot molten salt tank foundation is approximately 1.3 m depth. A Firelite refractory concrete upper layer with added steel fibers reduces the possibilities of tank movement. The lower layer is based on expanded clay aggregate. Supporting hoops hold a metallic ring that contains the compacted light expanded clay aggregate. At the bottom, the natural soil was compacted in order to increase its load-bearing capacity. Since this is a complex structure, its mean thermal conductivity was experimentally calibrated. The lumped mean thermal conductivity of the insulation and the aluminum jacket was also experimentally calibrated. The calibration process is described in Sec. 3.1.

The molten salt is the solar salt (60 % NaNO_3 and 40 % KNO_3), nitrogen gas is injected inside the tank in order to render both fluids inert. Tank pressure is automatically controlled to an established reference value. Such value is given in Tab. 1.

2. Tank Modeling

This section deals with the modeling of the tank. The modeling language and tool used to develop the model are briefly described in Sec. 2.1. Sec. 2.2 presents an overview of the tank model, whereas Sec. 2.3 to Sec. 2.11 introduce in detail each one of the components and processes that make up the model.

2.1. Modeling Language and Tool

The Modelica language [24] has been used for the modeling of the tank. Modelica was developed and is maintained by the Modelica Association, a non-profit and non-governmental international association. This modeling language has been designed to model conveniently complex physical systems because the language supports the object-oriented and the equation-based paradigms, together with advanced features such as, heat and flow connectors, constructions for tackling the initialization problem, support of events, advanced parametrization, etc. The Modelica tool used for the implementation is Dymola [10].

2.2. Overview of the Dynamic Tank Model

The tank has been modeled considering different subsystems. The liquid inside the tank has been modeled as a single Control Volume (CV) since the goal is to have a representative mean temperature value. The lumped liquid CV exchanges heat with the gas and the metallic structure. The gas inside the tank has been also modeled as a single lumped CV. The metallic structure has been divided in several parts: the roof, the floor and the wall in contact with liquid (wet wall) and the remaining wall which is in contact with gas (dry wall). The metallic structure also exchanges heat with the thermal insulation and the tank foundation. In the same way, the insulation is divided in roof insulation, wet and dry wall insulation. The insulation additionally exchanges heat with the aluminum jacket. The jacket exchanges heat with the ambient, whereas the tank foundation exchanges heat through conduction with the ground. To sum up, the tank model calculates the mass balances of liquid and gas, and the heat balances between liquid, gas, metallic structure, insulation, foundation and the environment.

Fig. 3 shows the icon of the tank model. This figure also shows the model inputs, two of them are the liquid inlet temperature and mass flow rate ($T_{l,ch}$, $\dot{m}_{l,ch}$). The liquid entrance to the tank has been modeled considering an ideal pump. The remaining inputs are the inlet temperature and pressure of the inert gas ($T_{g,ch}$, p_t), ambient and ground temperatures (T_{amb} , T_{grd}).

Since the pressure in the tank is controlled by a pressure relief valve and there is neither a tank pressure sensor nor flow meters for injected and expelled nitrogen in the hot molten salt tank, the tank pressure is assumed to be the nominal one at all times, this value is given in Tab. 1.

The following subsections introduce each one of the subsystems and other aspects about the model. Sec. 2.3 describes basic considerations about geometry. Fluids and their thermodynamic properties are defined in Sec. 2.4. Sec. 2.5 and 2.6 describes the governing equations for the liquid and gas CVs. Tank metallic structure, pump and insulation are described in Sec. 2.7, 2.8 and 2.9, respectively. Sec. 2.10 summarized all the used expressions for heat transfer, therefore all the heat flow rates (\dot{Q}) in previous equations are defined in this section. Finally, initial conditions required to solve the initialization problem are discussed in Sec. 2.11.

2.3. Geometry

Surface areas and volumes of the metallic structure and insulation for wall, roof and floor are calculated from manufacturer data according to Tab. 1. However, the model distinguishes between surfaces in contact with liquid and gas (wall and floor, it is assumed that the liquid never reaches the roof), for this reason the level (l), cross-sectional area (A_l) and volume (V_l) of the liquid inside the tank must be dynamically calculated.

The liquid level and cross-sectional area in the tank are calculated solving the system of Eqs. 1 and 2, since the volume is calculated from mass and density as described in Sec. 2.5. A_t and A_p are the tank and pump cross-sectional areas

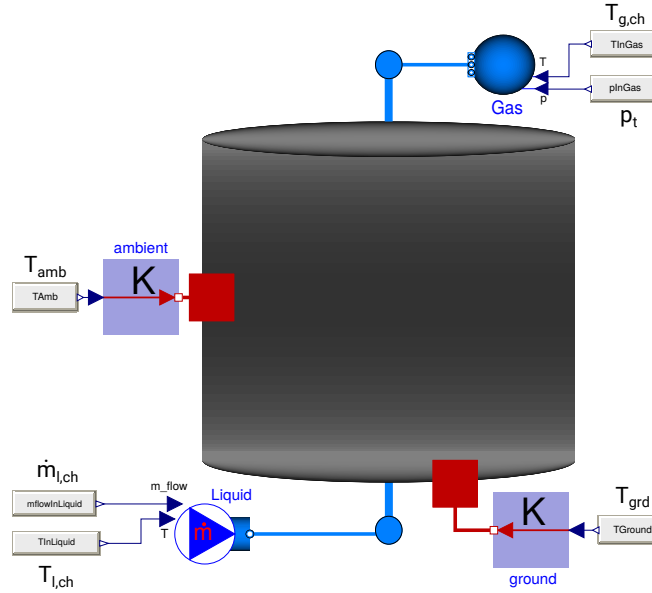


Figure 3: Model icon and inputs

and A_b is the liquid cross-sectional area over the inclined based, its diameter can be calculated by $d_b = l \cdot \tan(\alpha)$ when $l < L_b$ (see Fig. 2).

$$A_l = \begin{cases} A_b & \text{if } l < L_b, \\ A_t & \text{if } l \geq L_b \text{ and } l \leq L_{t2} - L_p, \\ A_t - A_p & \text{otherwise,} \end{cases} \quad (1)$$

$$V_l = A_l \cdot l. \quad (2)$$

2.4. Fluids

The following fluids are considered in the tank model, however they can be easily changed in the model by other fluids in the Modelica Media library [6] or new implemented models which takes into account this library interface.

- *Liquid.* Molten salts, in particular solar salt (60% NaNO_3 and 40% KNO_3). Its thermodynamic properties are available in [43, 12] and are calculated from molten salt temperature (T_{ms}).
- *Gas.* Nitrogen is the inert gas in the facility. This medium is included in the Modelica Media library. Its thermodynamic properties are based on [22] and are calculated from gas temperature (T_{gas}) and pressure (p_t).
- *Ambient fluid.* Dry air is the ambient fluid in the model. This medium is also included in Modelica Media and its thermodynamic properties are

based on the same reference than for nitrogen besides dynamic viscosity and thermal conductivity, which are calculated according to [38]. They are calculated from ambient temperature (T_{amb}), which is a model input, and pressure (p_{amb}), which is assumed constant and it is a model parameter (see Tab. 1).

2.5. Liquid Control Volume

The rate of change in liquid mass is given by the dynamic mass balance equation, Eq. 3, since there is only one inlet/outlet channel. If mass is entering the CV its sign is positive and it is negative otherwise.

$$\frac{dm_l}{dt} = \dot{m}_{l,ch}. \quad (3)$$

The rate of change in energy is derived from the general dynamic energy balance equation, Eq. 4. This equation can be simplified as Eq. 5 considering only internal and flow energies, heat transfer and work.

$$\frac{dE_l}{dt} = \dot{E}_{l,ch} - \dot{E}_{loss}, \quad (4)$$

$$\frac{dU_l}{dt} = \dot{m}_{l,ch}(u_{l,ch} + p_{l,ch}v_{l,ch}) + \dot{Q}_l - \dot{W}_l. \quad (5)$$

By means of the enthalpy definition ($h = u + pv$) and its time derivative together with the expansion work, as the only work done that affects the CV, Eq. 5 can be rewritten as Eq. 6.

$$\frac{dH_l}{dt} = \dot{m}_{l,ch}h_{l,ch} + V_l \frac{dp}{dt} + \dot{Q}_l. \quad (6)$$

Considering specific enthalpy, mass and assuming that the enthalpy only depends on temperature, Eq. 6 can be defined as Eq. 7, where C is the heat capacity ($C = mc_p$) and volume is calculated from mass and density.

$$C_l \frac{dT_l}{dt} = \dot{m}_{l,ch}(h_{l,ch} - h_l) + V_l \frac{dp}{dt} + \dot{Q}_l. \quad (7)$$

Eqs. 3 and 7 are the governing equations in the liquid CV, where mass (m_l) and temperature (T_l) are the state variables. When mass is entering the CV, i.e. $\dot{m}_{l,ch} > 0$, $h_{l,ch}$ is that from the incoming flow, otherwise $h_{l,ch} = h_l$.

2.6. Gas Control Volume

The gas CV governing equations were derived in the same way as for the liquid CV, therefore the mass and energy balance equations are given by Eqs. 8 and 9. The state variables are mass (m_g) and temperature (T_g). Additionally, the ideal-gas equation of state, Eq. 10, is also considered. Eqs. 8, 9 and 10 calculate $\dot{m}_{g,ch}$, T_g and m_g , respectively.

$$\frac{dm_g}{dt} = \dot{m}_{g,ch}, \quad (8)$$

$$C_g \frac{dT_g}{dt} = \dot{m}_{g,ch} (h_{g,ch} - h_g) + V_g \frac{dp}{dt} + \dot{Q}_g, \quad (9)$$

$$pV_g = m_g \frac{R_u}{M_g} T_g. \quad (10)$$

2.7. Metallic Structure

The energy balance for the metallic structure is modeled from Eq. 7 but considering that there is no mass transfer and assuming constant pressure, with these assumptions yields Eqs. 11, 12, 13 and 14, for the tank wet wall, dry wall, roof and floor, respectively.

$$C_{w,l} \frac{dT_{w,l}}{dt} = \dot{Q}_{w,l}, \quad (11) \quad C_{w,g} \frac{dT_{w,g}}{dt} = \dot{Q}_{w,g}, \quad (12)$$

$$C_{w,r} \frac{dT_{w,r}}{dt} = \dot{Q}_{w,r}, \quad (13) \quad C_{w,f} \frac{dT_{w,f}}{dt} = \dot{Q}_{w,f}. \quad (14)$$

Heat capacities are calculated from volumes, densities and specific heat capacities; the last two are assumed as constants values based on data provided by the manufacturer, their values are given in Tab. 1.

2.8. Vertical Pump

The modeling of the vertical pump is simplified assuming a vertical cylinder with the pump length and an equivalent diameter to the mean pump cross-sectional area. The energy balance equations for the wet and dry parts of the pump are modeled in the same way as the metallic structure. They are given by Eqs. 15 and 16. Pump dimensions, density and specific heat capacity are given in Tab. 1.

$$C_{p,l} \frac{dT_{p,l}}{dt} = \dot{Q}_{p,l}, \quad (15) \quad C_{p,g} \frac{dT_{p,g}}{dt} = \dot{Q}_{p,g}. \quad (16)$$

2.9. Thermal Insulation

The energy balance for the thermal insulation has been modeled in the same way as for the metallic structure, as shown in Eqs. 17, 18 and 19, for dry wall, wet wall and roof respectively. Values to calculate heat capacities are given in Tab. 1.

$$C_{i,l} \frac{dT_{i,l}}{dt} = \dot{Q}_{i,l}, \quad (17) \quad C_{i,g} \frac{dT_{i,g}}{dt} = \dot{Q}_{i,g}, \quad (18) \quad C_{i,r} \frac{dT_{i,r}}{dt} = \dot{Q}_{i,r}. \quad (19)$$

2.10. Heat Transfer

A sketch of the heat transfer processes considered in the tank model is depicted in Fig. 4. Nevertheless and in order to simplify the model, not all the heat transfer processes have been considered, see Tab. 3 for further details, the following assumptions were made.

- Mean values for thermodynamic properties in each volume of the model.
- Conductive heat transfer between the pump and the tank roof is neglected.
- Gas is a non-participating medium; neither emits, absorbs nor scatters radiation.
- Conduction in the tank metallic structure and between it and the inner insulation layer is assumed infinite in the radial direction and zero otherwise for the walls. It is infinite in the axial direction and zero otherwise for the floor and roof.
- Conduction in the pump is infinite in the axial direction and it is zero otherwise.
- Conduction in the insulation together with the aluminum jacket is dynamically calculated in the radial direction and is zero otherwise for the walls. It is also dynamically calculated in the axial direction and zero otherwise for the roof.
- Conduction in the foundation is dynamically calculated in the axial direction and it is zero otherwise.
- Radiation heat transfer between the aluminum jacket and the ambient is neglected.

Convective heat transfer was modeled considering a dynamic average convective heat transfer coefficient (α), the rate of heat transfer by convection from a surface of area (S_s) at uniform temperature (T_s) to the surrounding fluid at a uniform temperature (T_{fl}) is given by Newton's law of cooling, Eq. 20.

$$\dot{Q}_{conv,s,fl} = \alpha S_s (T_s - T_{fl}), \quad (20)$$

where the convective heat transfer coefficient can be calculated from empirical correlations for the Nusselt number (Nu) and Eq. 21, where L_c is the characteristic length and k_{fl} the fluid thermal conductivity.

$$Nu = \frac{\alpha L_c}{k_{fl}}. \quad (21)$$

Heat conduction in element i through a temperature difference in a layer of area S_i , thickness $L_{i,tck}$ with an average thermal conductivity k_i is calculated by

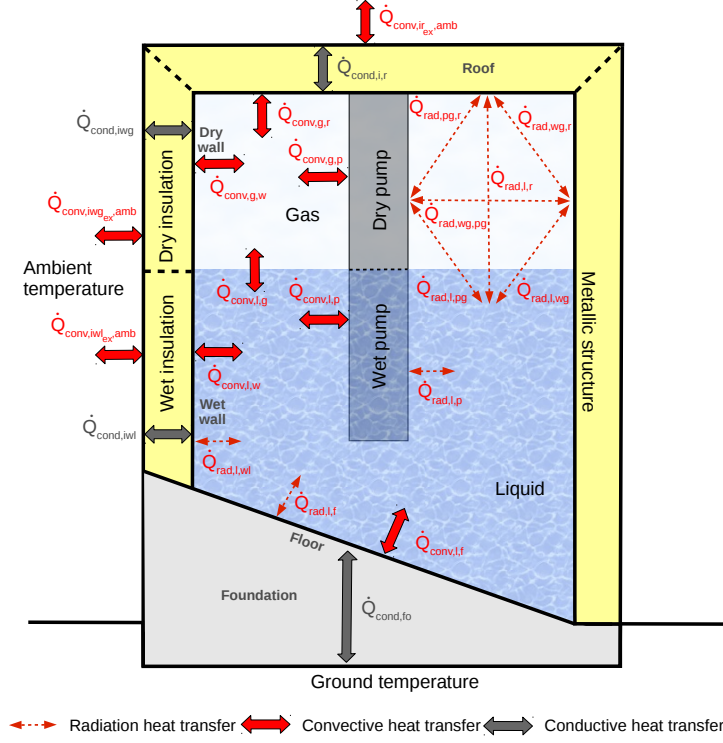


Figure 4: Heat transfer sketch

Fourier's law of heat conduction, Eq. 22, where $R_{i,cond}$ is the thermal resistance to conduction.

$$\dot{Q}_{cond,i} = \frac{T_{i,in} - T_{i,ex}}{\frac{L_{i,tck}}{k_i S_i}} = \frac{T_{i,in} - T_{i,ex}}{R_{cond,i}}. \quad (22)$$

When conduction dynamics are neglected, the temperature in a layer or between layers is the same. For instance, $T_{w,r} = T_{w,r,in} = T_{w,r,ex}$ for the mean, internal and external tank roof temperatures, and $T_{w,r,ex} = T_{i,r,in}$ for the external tank roof and internal insulation roof temperatures. When conduction dynamics are considered, it is assumed a linear temperature distribution in the layer, i.e. $T_{i,r} = 0.5(T_{i,r,in} + T_{i,r,ex})$ for roof insulation temperatures.

Radiation heat transfer in an enclosure consisting of two diffuse, gray and opaque surfaces of area S_1 and S_2 and constant emissivities ϵ_1 and ϵ_2 at uniform temperatures T_1 and T_2 can be calculated applying the network method [8]. The net rate of radiation heat transfer from surface 1 to surface 2 is determined by Eq. 23, where $E_{b,i} = \sigma T_i^4$ is the blackbody emissive power, F_{ij} is the view factor, and the R_{rad} terms are the thermal resistances to radiation.

$$\dot{Q}_{rad,12} = \frac{E_{b,1} - E_{b,2}}{R_{rad,1} + R_{rad,12} + R_{rad,2}} = \frac{\sigma(T_1^4 - T_2^4)}{\frac{1 - \epsilon_1}{S_1 \epsilon_1} + \frac{1}{S_1 F_{12}} + \frac{1 - \epsilon_2}{S_2 \epsilon_2}}. \quad (23)$$

In an analogous way, the network method can be applied for enclosures of n diffuse, gray and opaque surfaces. Each surface i must satisfy Eq. 24, where $J_i = \epsilon_i E_{b,i} + (1 - \epsilon_i)G_i$ denotes radiosity, being G_i the incident radiation.

$$\frac{E_{b,i} - J_i}{R_{rad,i}} = \sum_{j=1}^n \frac{J_i - J_j}{R_{rad,ij}}. \quad (24)$$

Since the previous equation must be satisfied by each surface, a system of n equations is obtained. From that system, radiosities (J_i) are normally calculated. Therefore, the rate of radiation from surface i to surface j can be determined from Eq. 25.

$$\dot{Q}_{rad,ij} = S_i F_{ij} (J_i - J_j) = \frac{J_i - J_j}{R_{rad,ij}}. \quad (25)$$

Each one of the heat transfer processes in the tank, depicted in Fig. 4 and summarized in Tab. 3 are described in the following subsections per tank component.

2.10.1. Liquid

The liquid inside the tank exchanges heat through natural convection with gas, floor, wet wall and wet pump and through radiation with wet wall, wet pump, wet floor, dry wall, dry pump and roof, therefore the net liquid heat flow rate (\dot{Q}_l) is calculated from Eq. 26.

$$\begin{aligned} \dot{Q}_l = & -\dot{Q}_{conv,l,g} - \dot{Q}_{conv,l,f} - \dot{Q}_{conv,l,w} - \dot{Q}_{conv,l,p} - \dot{Q}_{rad,l,wl} - \dot{Q}_{rad,l,pl} \\ & - \dot{Q}_{rad,l,f} - \dot{Q}_{rad,l,wg} - \dot{Q}_{rad,l,pg} - \dot{Q}_{rad,l,r}. \end{aligned} \quad (26)$$

Natural convection. The Nusselt number for natural convection between the upper liquid surface in contact with gas ($\dot{Q}_{conv,l,g}$) is given by Eqs. 27 and 28, as a function of the value of the Rayleigh number (Ra). These correlations are appropriate for hot surfaces facing upwards [8], where the characteristic length is $L_c = A_l/P_l$.

$$Nu = 0.54Ra^{1/4}, \quad 10^4 \leq Ra \leq 10^7, \quad (27)$$

$$Nu = 0.15Ra^{1/3}, \quad 10^7 < Ra \leq 10^{11}. \quad (28)$$

Natural convection between the liquid and the floor ($\dot{Q}_{conv,l,f}$) can be calculated with a Nusselt correlation for hot surfaces facing downwards [8], Eq. 29, with the same characteristic length as for the previous Nusselt correlation.

$$Nu = 0.27Ra^{1/4}, \quad 10^5 \leq Ra \leq 10^{11}. \quad (29)$$

Table 3: Heat transfer processes in the tank

Elements		Type	Modeled
Liquid CV	Gas	Convection	$\dot{Q}_{conv,l,g}$
	Inner wet wall	Convection	$\dot{Q}_{conv,l,w}$
		Radiation	$\dot{Q}_{rad,l,wl}$
	Outer wet pump	Convection	$\dot{Q}_{conv,l,p}$
		Radiation	$\dot{Q}_{rad,l,pl}$
	Inner floor	Convection	$\dot{Q}_{conv,l,f}$
		Radiation	$\dot{Q}_{rad,l,f}$
	Inner dry wall	Radiation	$\dot{Q}_{rad,l,wg}$
Outer dry pump	Radiation	$\dot{Q}_{rad,l,pg}$	
Inner roof	Radiation	$\dot{Q}_{rad,l,r}$	
Gas CV	Inner dry wall	Convection	$\dot{Q}_{conv,g,w}$
	Outer dry pump	Convection	$\dot{Q}_{conv,g,p}$
	Inner floor	Convection	$\dot{Q}_{conv,g,f}$
	Inner roof	Convection	$\dot{Q}_{conv,g,r}$
Inner dry wall	Outer dry pump	Radiation	$\dot{Q}_{rad,wg,pg}$
	Inner roof	Radiation	$\dot{Q}_{rad,wg,r}$
	Inner floor	Radiation	Neglected
Outer dry pump	Inner roof	Radiation	$\dot{Q}_{rad,pg,r}$
		Conduction	Neglected
	Inner floor	Radiation	Neglected
Inner metal	Outer metal	Roof	Conduction Axial ¹
		Dry wall	Conduction Radial ²
		Wet wall	Conduction Radial ²
		Dry pump	Conduction Radial ²
		Wet pump	Conduction Radial ²
		Floor	Conduction Axial ¹
Outer metal	Inner insulation	Roof	Conduction Axial ¹
		Dry wall	Conduction Radial ²
		Wet wall	Conduction Radial ²
	Inner foundation	Floor	Conduction Axial ¹
Inner insulation	Outer jacket	Roof	Conduction $\dot{Q}_{cond,ir}$
		Dry wall	Conduction $\dot{Q}_{cond,iwg}$
		Wet wall	Conduction $\dot{Q}_{cond,iwl}$
Inner foundation	Outer foundation	Floor	Conduction $\dot{Q}_{cond,fo}$
Outer jacket	Ambient	Roof	Convection $\dot{Q}_{conv,ir_{ex},amb}$
			Radiation Neglected
		Dry wall	Convection $\dot{Q}_{conv,iwg_{ex},amb}$
			Radiation Neglected
		Wet wall	Convection $\dot{Q}_{conv,iwl_{ex},amb}$
			Radiation Neglected

¹ Infinite in axial direction, zero otherwise.² Infinite in radial direction, zero otherwise.

The average Nusselt number for natural convection between liquid and wet wall ($\dot{Q}_{conv,l,w}$) can be calculated from an empirical correlation for a fluid in contact with a vertical plate, Eq. 30 [8], where Pr is the Prandtl number. A vertical cylinder can be considered as a vertical plate as long as the diameter of the cylinder is large enough so the curvature effects are negligible. This assumption holds when $d \geq 35L_c/Gr^{1/4}$ [8]. Gr is the Grashof number and L_c is the characteristic length which in this case is the vertical length of the cylinder.

$$Nu = \left(0.825 + \frac{0.387Ra^{1/6}}{\left(1 + \left(\frac{0.492}{Pr}\right)^{9/16}\right)^{8/27}} \right)^2. \quad (30)$$

For slender cylinders that do not satisfy the abovementioned condition, there are also Nusselt correlations in the literature [27]. This is the case for the laminar natural convection between liquid and wet pump ($\dot{Q}_{conv,l,p}$). The Nusselt correlation in Eq. 31 [7] is used in this case, where Nu_{vp} is the average Nusselt number for a vertical flat plate, which can be calculated by Eq. 30.

$$Nu = Nu_{vp} \left(1 + 0.3 \left(32^{0.5} + Gr^{-0.25} \frac{L}{d} \right)^{0.909} \right). \quad (31)$$

Radiation. Radiation heat flow rates between liquid and wet elements: floor ($\dot{Q}_{rad,l,f}$), wall ($\dot{Q}_{rad,l,wl}$) and pump ($\dot{Q}_{rad,l,pl}$) are modeled considered an enclosure of only two surfaces: the liquid and the element, according to Eq. 23, since both elements are in contact the view factor is 1, $F_{l,f} = F_{l,wl} = F_{l,p} = 1$. Wet wall and floor surface areas are calculated as a function of the level. Constant mean emissivities for the different elements are given in Tab. 1.

Radiation heat transfer between liquid and dry elements was calculated considering the case of enclosures with four surfaces: liquid, dry wall, dry pump and roof. Radiosities (J_l, J_{wg}, J_{pg}, J_r) are calculated from the system of equations obtained after applying Eq. 24 for each enclosure surface, Eqs. 32, 33, 34 and 35.

$$\frac{E_{b,l} - J_l}{R_{rad,l}} = \frac{J_l - J_{wg}}{R_{rad,l,wg}} + \frac{J_l - J_{pg}}{R_{rad,l,pg}} + \frac{J_l - J_r}{R_{rad,l,r}}, \quad (32)$$

$$\frac{E_{b,wg} - J_{wg}}{R_{rad,wg}} = \frac{J_{wg} - J_l}{R_{rad,wg,l}} + \frac{J_{wg} - J_{pg}}{R_{rad,wg,pg}} + \frac{J_{wg} - J_r}{R_{rad,wg,r}}, \quad (33)$$

$$\frac{E_{b,pg} - J_{pg}}{R_{rad,pg}} = \frac{J_{pg} - J_l}{R_{rad,pg,l}} + \frac{J_{pg} - J_{wg}}{R_{rad,pg,wg}} + \frac{J_{pg} - J_r}{R_{rad,pg,r}}, \quad (34)$$

$$\frac{E_{b,r} - J_r}{R_{rad,r}} = \frac{J_r - J_l}{R_{rad,r,l}} + \frac{J_r - J_{wg}}{R_{rad,r,wg}} + \frac{J_r - J_{pg}}{R_{rad,r,pg}}. \quad (35)$$

In order to solve the previous system of equations, the thermal resistance to radiation terms (R_{rad}) require surface areas, emissivities and view factors. The liquid, dry wall and dry pump surface areas depend on the liquid level, the roof surface area is constant. Mean emissivity values are given in Tab. 1.

View factors are calculated, first considering the summation rules for each surface: liquid (Eq. 36), dry wall (Eq. 37), dry pump (Eq. 38) and roof (Eq. 39),

$$F_{l,l} + F_{l,wg} + F_{l,pg} + F_{l,r} = 1, \quad (36) \quad F_{wg,l} + F_{wgl,wg} + F_{wg,pg} + F_{wg,r} = 1, \quad (37)$$

$$F_{r,l} + F_{r,wg} + F_{r,pg} + F_{r,r} = 1, \quad (38) \quad F_{pg,l} + F_{pg,wg} + F_{pg,pg} + F_{pg,r} = 1, \quad (39)$$

second, the following relationships about view factors can be stated based on the tank geometry,

$$F_{l,l} = 0, \quad (40) \quad F_{pg,pg} = 0, \quad (41) \quad F_{r,r} = 0, \quad (42)$$

third, applying reciprocity rules,

$$S_l F_{l,wg} = S_{wg} F_{wg,l}, \quad (43) \quad S_l F_{l,pg} = S_{pg} F_{pg,l}, \quad (44)$$

$$S_l F_{l,r} = S_r F_{r,l}, \quad (45) \quad S_{wg} F_{wg,pg} = S_{pg} F_{pg,wg}, \quad (46)$$

$$S_{wg} F_{wg,r} = S_r F_{r,wg}, \quad (47) \quad S_{pg} F_{pg,r} = S_r F_{r,pg}. \quad (48)$$

From Eq. 36 to Eq. 48, it is obtained a system of thirteen equations with sixteen unknown view factors. Therefore, the fourth step is to estimate three of those view factors.

One of the calculated factors is the view factor from the dry pump to the roof ($F_{pg,r}$). It is estimated from the cylinder-disk view factor ($F_{cyl-disk}$), according to Eq. 49 [29]. Fig. 5 shows a sketch of surfaces 1 and 2, where $r_1 = d_p/2$ is the pump radius, $r_2 = d_{t,in}/2$ is the roof radius and $L_1 = \min(L_p, L_{t2} - l)$ is the dry pump length, see Fig. 2.

$$\begin{aligned} F_{cyl-disk}(L_1, r_1, r_2) &= \frac{1}{2\pi} \cos^{-1} \left(\frac{L_1^2 - r_2^2 + r_1^2}{L_1^2 + r_2^2 - r_1^2} \right) - \left(\frac{r_1}{2L_1} \right) \\ &\left(\left(\frac{(L_1^2 + r_2^2 + r_1^2)^2}{r_1^4} - 4 \left(\frac{r_1}{r_2} \right)^2 \right)^{1/2} \left(\cos^{-1} \left(\frac{r_1 (L_1^2 - r_2^2 + r_1^2)}{r_2 (L_1^2 + r_2^2 - r_1^2)} \right) \right) \right) \\ &+ \left(\frac{L_1^2 - r_2^2 + r_1^2}{r_1^2} \right) \sin^{-1} \frac{r_1}{r_2} - \left(\frac{\pi}{2} \right) \frac{L_1^2 - r_2^2 + r_1^2}{r_1^2}. \end{aligned} \quad (49)$$

Another calculated factor is the view factor from the dry pump to the dry wall ($F_{pg,wg}$). The view factor for concentric cylinders ($F_{cyl-cyl}$) is used according to Eq. 50, where L_1, r_1, r_2 have the same meaning than for the cylinder-disk view factor and $L_a = \max(0, L_{t2} - L_p - l)$ is the distance in height of the gap between the pump and the liquid surface. Surfaces 1 and 3 are shown in Fig. 5.

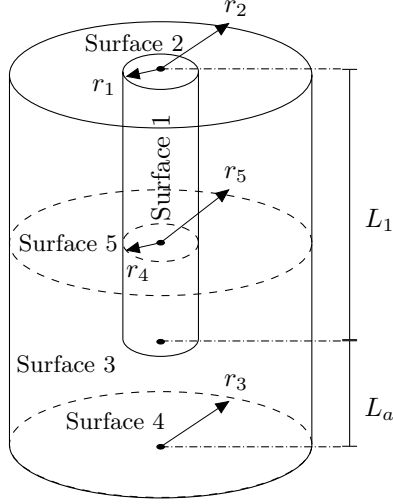


Figure 5: Geometry for view factors

This concentric cylinder structure corresponds to configuration III in [29], since there are different view factors depending on the relative position of the inner cylinder. $F_{cyl,disk}$ is the cylinder-disk view factor

$$\begin{aligned}
 F_{cyl-cyl}(L_1, L_a, r_1, r_2) &= 1 + \frac{L_a}{L_1} F_{cyl-disk}(L_a, r_1, r_2) - F_{cyl-disk}(L_1, r_1, r_2) \\
 &\quad - \frac{L_1 + L_a}{L_1} F_{cyl-disk}(L_1 + L_a, r_1, r_2).
 \end{aligned} \tag{50}$$

The last calculated view factor is that from the liquid to the roof ($F_{l,r}$). When the liquid level falls below the bottom of the pump ($L_a > 0$), this view factor is calculated from the expression from disk to a coaxial ring ($F_{disk-ring}$), Eq. 51 [16], where the only new term is r_3 which is the liquid equivalent hydraulic radius neglecting the tank inclination and assuming a uniform liquid distribution. Surfaces 2 and 4 are shown in Fig. 5.

$$\begin{aligned}
 R_{13} &= \frac{r_1}{r_3}, \quad R_{23} = \frac{r_2}{r_3}, \quad H_1 = \frac{r_1}{L_1 + L_a}, \\
 F_{disk-ring}(R_{13}, R_{23}, H_1) &= \frac{1}{2} \left(R_{23}^2 - R_{13}^2 - \left((1 + R_{23}^2 + H_1^2)^2 - 4R_{23}^2 \right)^{1/2} \right. \\
 &\quad \left. + \left((1 + R_{13}^2 + H_1^2)^2 - 4R_{13}^2 \right)^{1/2} \right),
 \end{aligned} \tag{51}$$

When the liquid level reaches the pump ($L_a = 0$), $F_{l,r}$ is calculated from the expression for parallel coaxial rings ($F_{disk-disk}$), Eq. 52 [16], where r_4 is the

pump radius and r_5 is the tank radius. Surfaces 1 and 5 are depicted in Fig. 5. Notice that Eq. 52 is a general expression, but in our particular case $r_1 = r_4$ and $r_2 = r_5$, therefore $R_{14} = 1$ and $R_{51} = R_{21}$.

$$\begin{aligned}
R_{51} &= \frac{r_5}{r_4}, \quad R_{14} = \frac{r_1}{r_4} = 1, \quad R_{21} = \frac{r_2}{r_1}, \quad H_2 = \frac{r_1}{L}, \\
F_{disk-disk}(R_{51}, R_{14}, R_{21}, H_2) &= \frac{1}{2(R_{51}^2 - 1)} \left(\left((R_{51}^2 + R_{14}^2 + H_2^2)^2 \right. \right. \\
&\quad \left. \left. - (2R_{14}R_{51})^2 \right)^{1/2} \right. \\
&\quad \left. - \left((R_{51}^2 + R_{21}^2 + H_2^2)^2 - (2R_{51}R_{21})^2 \right)^{1/2} \right. \\
&\quad \left. + \left((1 + R_{21}^2 + H_2^2)^2 - (2R_{21})^2 \right)^{1/2} \right. \\
&\quad \left. - \left((1 + R_{14}^2 + H_2^2)^2 - (2R_{14})^2 \right)^{1/2} \right). \quad (52)
\end{aligned}$$

Once view factors, thermal resistances to radiation and radiosities are computed, the rates of radiation heat transfer can be calculated from Eq. 25: $\dot{Q}_{rad,l,wg}$, $\dot{Q}_{rad,l,pg}$, $\dot{Q}_{rad,l,r}$, $\dot{Q}_{rad,wg,pg}$, $\dot{Q}_{rad,wg,r}$ and $\dot{Q}_{rad,pg,r}$.

If the pump is excluded from the heat transfer analysis, there would be only necessary to calculate two view factors instead of three. In that case, the view factor from the liquid to the roof would be calculated by the view factor expression for parallel coaxial disk [8]. The view factor from the dry wall to itself would be calculated by means of the view factor expression for the cylinder inner surface [37].

2.10.2. Gas

Assuming that the gas is a non-participating medium, gas exchanges heat only through natural convection (\dot{Q}_g) with liquid, roof, dry wall, dry pump and floor according to Eq. 53.

$$\dot{Q}_g = \dot{Q}_{conv,l,g} - \dot{Q}_{conv,g,w} - \dot{Q}_{conv,g,p} - \dot{Q}_{conv,g,r} - \dot{Q}_{conv,g,f}. \quad (53)$$

$\dot{Q}_{conv,l,g}$ was calculated by Eqs. 27 and 28, whereas $\dot{Q}_{conv,g,w}$ and $\dot{Q}_{conv,g,p}$ can be calculated by means of Eq. 30 and Eq. 31, respectively. When gas is in contact with the tank floor (i.e. $L < L_b$), natural convection heat transfer between the gas and the floor ($\dot{Q}_{conv,g,f}$) can be calculated by Eq. 29, where the heat exchange area is $S_{f,g} = A_t - A_b$ (see Fig. 2), the characteristic length is $L_c = A_g/P_g$ and the perimeter (P_g) may be calculated once an equivalent diameter of A_g is obtained.

2.10.3. Metallic Structure

Heat flow rates for the metallic structure: floor, roof, wet and dry walls, are given by Eqs. 54, 55, 56 and 57, respectively. All terms in those equations have

been previously introduced, beside conductive heat flow rates in the thermal insulation and foundation which are detailed in Sec. 2.10.5 and 2.10.6.

$$\dot{Q}_{w,f} = \dot{Q}_{conv,l,f} + \dot{Q}_{rad,l,f} + \dot{Q}_{conv,g,f} - \dot{Q}_{cond,fo}, \quad (54)$$

$$\dot{Q}_{w,r} = \dot{Q}_{conv,g,r} + \dot{Q}_{rad,l,r} + \dot{Q}_{rad,wg,r} + \dot{Q}_{rad,pg,r} - \dot{Q}_{cond,ir}, \quad (55)$$

$$\dot{Q}_{w,l} = \dot{Q}_{conv,l,w} + \dot{Q}_{rad,l,wl} - \dot{Q}_{cond,iwl}, \quad (56)$$

$$\dot{Q}_{w,g} = \dot{Q}_{conv,g,w} + \dot{Q}_{rad,l,wg} - \dot{Q}_{rad,wg,pg} - \dot{Q}_{rad,wg,r} - \dot{Q}_{cond,iwg}. \quad (57)$$

2.10.4. Vertical Pump

Wet and dry pump heat flow rates are given by Eqs. 58 and 59, where all the terms have been previously introduced.

$$\dot{Q}_{p,l} = \dot{Q}_{conv,l,p} + \dot{Q}_{rad,l,pl}, \quad (58)$$

$$\dot{Q}_{p,g} = \dot{Q}_{cov,g,p} + \dot{Q}_{rad,l,pg} + \dot{Q}_{rad,wg,pg} - \dot{Q}_{rad,pg,r}. \quad (59)$$

2.10.5. Insulation

Aluminum jacket heat conduction is lumped together the insulation heat conduction, radiation heat transfer between the outer jacket layer and the ambient has been neglected. Therefore, thermal insulation heat flow rates are by means of conduction from the internal to the external layer and by convection with the ambient, Eqs. 60, 61 and 62.

$$\dot{Q}_{i,r} = \dot{Q}_{cond,ir} - \dot{Q}_{conv,ir_{ex},amb}, \quad (60)$$

$$\dot{Q}_{i,wl} = \dot{Q}_{cond,iwl} - \dot{Q}_{conv,iwl_{ex},amb}, \quad (61)$$

$$\dot{Q}_{i,wg} = \dot{Q}_{cond,iwg} - \dot{Q}_{conv,iwg_{ex},amb}. \quad (62)$$

Conduction. Insulation conductive heat flow rates (Eq. 22) are calculated from thermal resistances for roof, dry wall and wet wall given by Eqs. 63, 64 and 65. Wall surfaces areas are calculated according to the tank level. Thermal conductivities and insulation thicknesses are given in Tab. 1.

$$R_{cond,ir} = \frac{L_{tck,i}}{k_i S_{ir}}, \quad (63) \quad R_{cond,iwg} = \frac{L_{tck,i}}{k_i S_{iwg}}, \quad (64)$$

$$R_{cond,iwl} = \frac{L_{tck,i}}{k_i S_{iwl}}. \quad (65)$$

Natural convection. Average Nusselt numbers for natural convection between ambient and wall insulation ($\dot{Q}_{conv,iwl_{ex},amb}$ and $\dot{Q}_{conv,iwg_{ex},amb}$) can be calculated from Eq. 30, whereas for the roof ($\dot{Q}_{conv,ir_{ex},amb}$), Eqs. 27 and 28 can be used.

2.10.6. Foundation

For the foundation, heat flow rate is by means of conduction, Eq. 66, considering the metallic tank floor and ground temperatures. Thermal resistance to

Table 4: Tank model state variables

State	Description	State	Description
m_l	Liquid mass	$T_{w,f}$	Tank floor temperature
m_g	Gas mass	$T_{p,l}$	Wet pump temperature
T_l	Liquid temperature	$T_{p,g}$	Dry pump temperature
T_g	Gas temperature	$T_{i,l}$	Wet wall insulation temperature
$T_{w,l}$	Wet wall temperature	$T_{i,g}$	Dry wall insulation temperature
$T_{w,g}$	Dry wall temperature	$T_{i,r}$	Insulation roof temperature
$T_{w,r}$	Tank roof temperature		

conduction is given by Eq. 67. Thermal conductivity, thickness and dimensions to calculate the surface area are given in Tab. 1.

$$\dot{Q}_{fo} = -\dot{Q}_{cond,fo}, \quad (66) \quad R_{cond,fo} = \frac{L_{tck,fo}}{k_{fo}S_{fo}}. \quad (67)$$

2.11. Initialization and Initial Conditions

The initialization involves providing suitable initial values to the state variables. State variables were defined from Sec. 2.5 to Sec. 2.9. They are summarized in Tab. 4. The default initial conditions require only three values: initial liquid level, initial liquid and gas temperature, although other initial conditions can be also easily set in the model if needed.

If the liquid level is not zero, the liquid temperature is used to initialize the following temperatures: liquid, wet wall, wet pump and floor, otherwise the gas temperature is used. The temperatures of the dry wall, dry pump, roof and gas are initialized with the gas temperature. The time derivatives of the insulation temperatures in roof, wet wall and dry wall are set to zero. Initial liquid mass is calculated from the initial liquid level and the initial liquid temperature, whereas initial gas mass is calculated from the initial liquid level and gas temperature.

3. Simulation, Calibration and Validation

This section deals with model simulations. Sec. 3.1 shows the calibration of unknown parameters, mean thermal conductivities of the tank insulation and foundation in our case. Sec. 3.2 presents the model validation in charging and discharging processes, as well as at predicting thermal losses dynamics. Sec. 3.3 introduces an open source TES tank simulation application which reproduces the validation cases considered in Sec. 3.2 and it is freely available. The following inputs must be provided to the model to be able to perform the simulations, as previously shown in Fig. 3.

- Molten salt inlet temperature and mass flow rate $(T_{l,ch}, \dot{m}_{l,ch})$.
- Gas inlet temperature $(T_{g,ch})$.
- Controlled tank pressure (p_t) .

- Ambient temperature (T_{amb}).
- Ground temperature (T_{grad}).

An experimental campaign was performed in order to calibrate and validate the tank model, experimental data are available for $T_{l,ch}$, $\dot{m}_{l,ch}$ and T_{amb} . Gas inlet temperature ($T_{g,ch}$) is assumed to be the same as ambient temperature (T_{amb}). Tank pressure (p_t) is assumed to be the nominal one at all times, this value is given in Tab. 1. Ground temperature (T_{grad}) beyond a depth of 1 m is usually insensitive to the diurnal cycle of air temperature and solar radiation, therefore a mean ground temperature value for each experiment is assumed depending on the month where the experiment was performed and according to the data provided in [13].

Once a simulation is performed, the most important output variables, which can be compared with experimental data, are: molten salt level (l), mean molten salt temperature ($T_{l,sim}$) and mean gas temperature ($T_{g,sim}$).

3.1. Calibration

Mean insulation and aluminum jacket thermal conductivity, together with mean foundation thermal conductivity, are the parameters that have been calibrated from experimental data. The optimization problem can be formulated as simultaneously minimize the Root Mean Square (RMS) differences between experimental and simulated molten salt (ΔT_l) and gas (ΔT_g) temperatures, which are the objective functions, tuning both thermal conductivity parameters (k_i , k_{fo}), see Eq. 68, where n is the number of samples.

Experimental data from a thermal losses experiment, where the tank was previously charged with molten salt at high temperature and left at rest, was used. Experimental temperature values from the thermocouple closest to the arithmetic mean temperature of all thermocouples immersed in molten salt and exposed to the gas were used for $T_{l,exp}$ and $T_{g,exp}$ samples, respectively.

$$\begin{aligned}
\text{minimize} \quad & \Delta T_l = \sqrt{\frac{\sum_{i=1}^n (T_{l,exp}(i) - T_{l,sim}(i))^2}{n}}, \\
& \Delta T_g = \sqrt{\frac{\sum_{i=1}^n (T_{g,exp}(i) - T_{g,sim}(i))^2}{n}}, \tag{68} \\
\text{with respect to} \quad & k_i \in \mathbb{R}, \\
& k_{fo} \in \mathbb{R}, \\
\text{subject to} \quad & 0 \leq k_i \leq 1, \\
& 0 \leq k_{fo} \leq 1.
\end{aligned}$$

In order to solve this problem, an open source multi-platform optimization software tool, which is being developed by the authors, was used. This tool allows the user to perform parameter optimization and estimation studies in Functional Mock-up Interface (FMI) compliant models [3]. FMI is a tool

independent standard to support both model exchange and co-simulation of dynamic models [25]. Most Modelica tools support exporting Modelica models to Functional Mock-up Units (FMUs). A FMU is a FMI compliant model.

The optimization software tool uses the FMI++ library [40] for simulation and a Multi-Objective Genetic Algorithm (MOGA) from the Sandia-developed JEGA library included in the Dakota toolkit [1]. More details about the design of the optimization tool and how to use it can be found in [3].

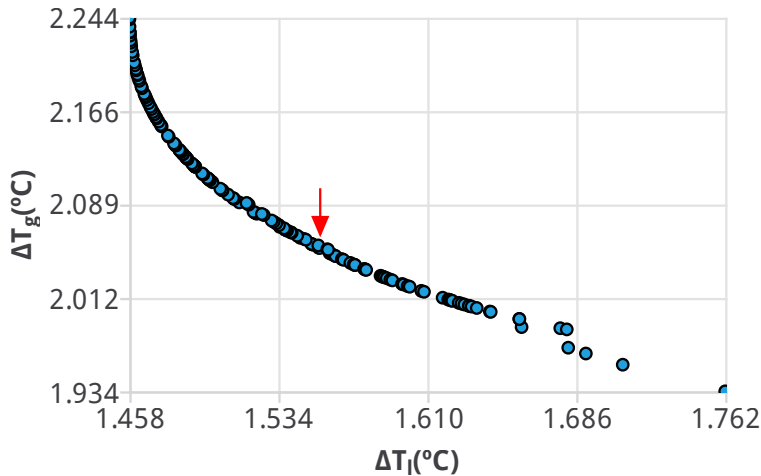


Figure 6: Tank model calibration Pareto front

The MOGA algorithm provides solutions in or close to the Pareto front, that is a set of nondominated solutions which are chosen as optimal because no objective can be improved without worsen at least one of the remaining objectives. Fig. 6 shows the Pareto front of our optimization problem, where axes' values are the values of both objective functions (ΔT_l , ΔT_g). The solution pointed by the arrow in Fig. 6 is the selected one, which corresponds to the minimum solution of a single objective function (ΔT) adding up both original objective functions (ΔT_l , ΔT_g) with same weights (w_l , w_g), i.e. $\Delta T = w_l \Delta T_l + w_g \Delta T_g$, where $w_l = w_g$. In the selected solution, the objective function values are $\Delta T_l = 1.554^\circ\text{C}$ and $\Delta T_g = 2.053^\circ\text{C}$ and the estimated parameter values are $k_i = 0.240 \text{ W}/(\text{m K})$ and $k_{fo} = 0.466 \text{ W}/(\text{m K})$.

3.2. Validation

This section compares data from the experimental campaign with simulation results in three different scenarios from Sec. 3.2.2 to Sec. 3.2.4. Measurement uncertainty are analyzed in Sec. 3.2.1.

Dymola [10] has been the Modelica tool used for the dynamic simulations in this section. The numerical solver used was DASSL [26], a variable-step

Table 5: Thermocouple uncertainty sources

Source	Type	Value	Prob. dist.	Divisor	Abs. std. uncertainty
Thermal camera	Standard	0.287 °C	Normal	1	0.287 °C
Digital therm.	Standard	0.064 °C	Normal	1	0.064 °C
Dry-well cal.	Tolerance	0.5 °C	Uniform	$\sqrt{3}$	0.29 °C

variable-order multistep solver in the numerical integration of Differential Algebraic Equation (DAE) systems, where the Newton iteration method is used to solve the resulting nonlinear algebraic system of equations at each time step. The absolute and relative tolerances were set to 10^{-4} . Simulations were performed in a conventional laptop (4 x Intel Core i5 2.60 GHz, 8 GBytes of RAM).

3.2.1. Measurement uncertainty

The thermocouples in the facility were calibrated with respect to a digital thermometer in a temperature dry-well calibrator. With the aim of fitting thermocouple temperatures to the digital thermometer temperatures, polynomial functions are used. The combined standard uncertainty of each thermocouple at 400 °C is $u(T) = 0.4$ °C. It is calculated considering the thermocouple uncertainty sources from Tab. 5, together with the uncertainty from the polynomial fitting to experimental data and software conversion and resolution, $u \approx 0.1$ °C. The combined standard uncertainty of the thermocouples may be slightly smaller at lower temperatures.

The volumetric vortex flow meter has a 1% tolerance at 4 m³/h and a 0.75% tolerance at 7 m³/h according to the manufacturer documentation.

3.2.2. Charging Process

The model is subjected to several inlet mass flow rate steps in this experiment, see Fig. 7, where the molten salt inlet temperature is also shown. The tank is empty at the beginning of the simulation, see Fig. 8. The tank metallic structure and gas temperatures are kept at a certain temperature by means of the heat tracing system in order to prevent molten salt freezing when feeding the tank. This temperature value is an initial condition of the model. This simulation is performed in less than 5 s.

Fig. 8 shows the experimental and simulated levels. Horizontal lines point out the position in height of the thermocouples, see Fig. 2. Take into account that thermocouples in the facility (Th 1 - Th 6) measure tank wall temperatures, which provide estimations for molten salt and gas temperatures. Fig. 9 shows experimental (thermocouples measuring the wet wall) and simulated molten salt temperatures. Notice that there is no experimental molten salt temperature until the tank level reaches the first thermocouple position, see Fig. 8. Fig. 10 shows experimental and simulated gas temperatures. Also notice that the molten salt level reaches the last thermocouple at the end of the simulation,

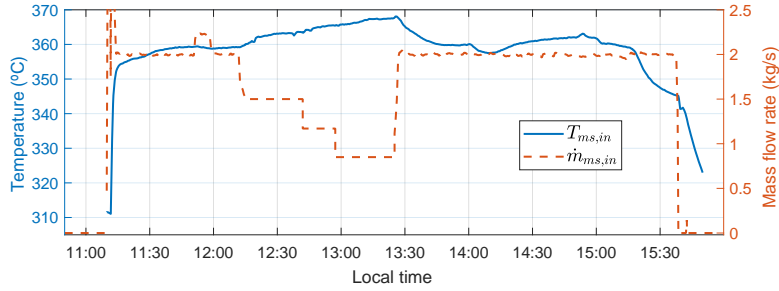


Figure 7: Charging process: inlet molten salt mass flow rate and temperature

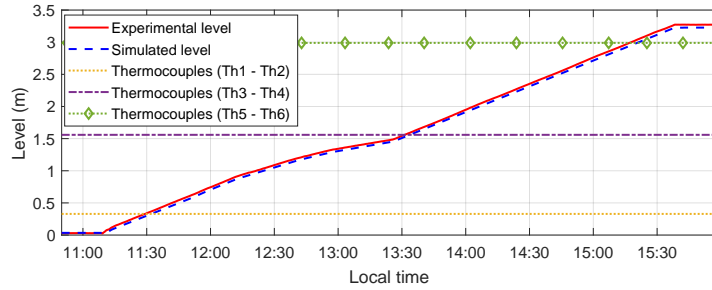


Figure 8: Charging process: experimental and simulated levels. The position of the thermocouples along the height of the tank is also represented

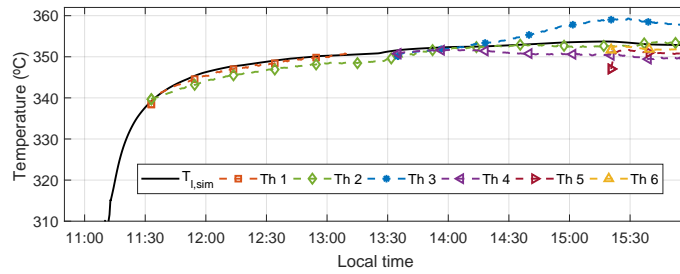


Figure 9: Charging process: experimental and simulated molten salt temperatures

therefore there are no available measurements for gas temperature, because the temperatures from the highest-placed thermocouples correspond to molten salt temperatures in this situation.

There is a good agreement between experimental and simulated level and molten salt temperature. The mean gas temperature is slightly underestimated, the RMS difference between the closest experimental (thermocouple 5) and sim-

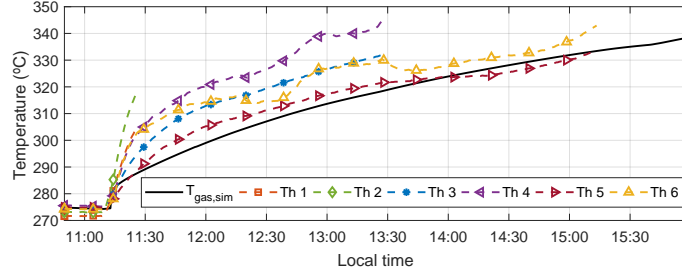


Figure 10: Charging process: experimental and simulated gas temperatures

ulated temperatures is 2.8 °C. The gas temperature dynamics properly match the experimental ones.

Fig. 11 shows the molten salt heat exchange in percentage with the remaining components inside the tank according to Eq. 26, i.e. the rate of heat exchange in percentage with floor, dry wall, wet wall, dry pump, wet pump and roof depending on the heat transfer process: convection or radiation. Fig. 12 shows the same information but for the gas according to Eq. 53. A positive heat flow rate means heat leaving the CV, whereas negative ones mean heat entering the CV.

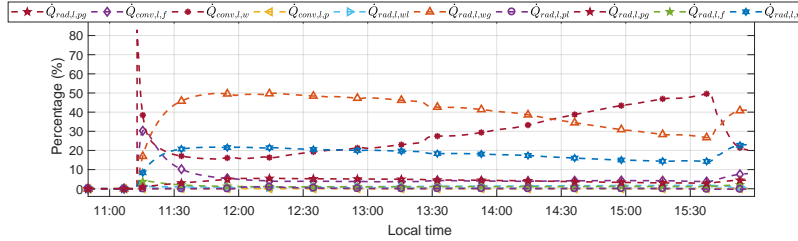


Figure 11: Charging process: molten salt heat flow rate

Fig. 11 shows that at the beginning of the simulation, when molten salts enter the tank, most heat transfer is due to convection with wet parts, floor and wall ($\dot{Q}_{conv,l,f}$ and $\dot{Q}_{conv,l,w}$). After that, radiation heat transfer with dry wall ($\dot{Q}_{rad,l,wg}$) and roof ($\dot{Q}_{rad,l,r}$) also plays an important role. Heat transfer by convection to the wet wall ($\dot{Q}_{conv,l,w}$) increases as the tank level rises up, at the same time that radiation with dry wall ($\dot{Q}_{rad,l,wg}$) decreases due to the reduction in the dry wall surface area. Radiation heat transfer with wet parts: floor ($\dot{Q}_{rad,l,f}$) and wet wall ($\dot{Q}_{rad,l,wl}$) is small in comparison to convective heat transfer ($\dot{Q}_{conv,l,f}$ and $\dot{Q}_{conv,l,w}$), therefore they may be neglected to simplify the model. In general, heat transfer with the pump only represents a small fraction ($\dot{Q}_{conv,l,p}$, $\dot{Q}_{rad,l,pl}$ and $\dot{Q}_{rad,l,pg}$) and it may be neglected also to simplify the

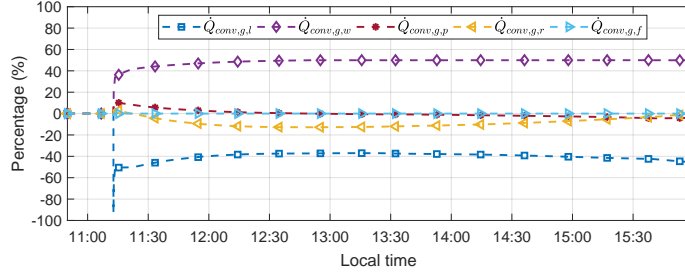


Figure 12: Charging process: gas heat flow rate

model. Although convective heat transfer with gas ($\dot{Q}_{conv,l,g}$) is small in terms of molten salt heat flow rate percentage, it represents the most relevant amount for the gas, as shown in Fig. 12.

With respect to the gas, most heat comes from molten salt by natural convection ($\dot{Q}_{conv,g,l}$). The gas also receives heat from the roof by natural convection ($\dot{Q}_{rad,g,r}$), which receives energy from molten salts by radiation ($\dot{Q}_{rad,l,r}$). On the other hand, the gas transfers a significant amount of heat to the dry wall ($\dot{Q}_{conv,g,wg}$), which is also heated by molten salts through radiation ($\dot{Q}_{rad,l,wg}$). Convective heat transfer with the floor ($\dot{Q}_{conv,g,f}$) and pump ($\dot{Q}_{conv,g,p}$) is small and it may be neglected to simplify the model.

3.2.3. Discharging Process

The tank discharging process was also simulated and compared against experimental data. Fig. 13 shows the outlet molten salt mass flow rate and temperature. Experimental and simulated levels, molten salt and gas temperatures are shown in Figs. 14, 15 and 16, respectively. Simulation results agree with experimental data as shown in figures. In Fig. 16, thermocouples exhibit a dynamic behavior related to the thermowells where they are installed, which is due to thermal inertia. This behavior is not related to gas temperature dynamics. After such transients, the dynamics are similar to those from the model. This simulation was also fast, it took less than 4 s.

3.2.4. Thermal losses

The experiment described in this section was conducted in order to estimate thermal losses. Thermal losses rate is an important factor in TES systems because molten salts must be kept above a certain minimum temperature in order to prevent their freezing. The developed tank model provides a unique mean molten salt temperature, however molten salts close to the tank floor may have a slightly lower temperature. Nevertheless, the mean temperature value provided by the model can be used as a reference for estimating the lowest molten salt tank temperature.

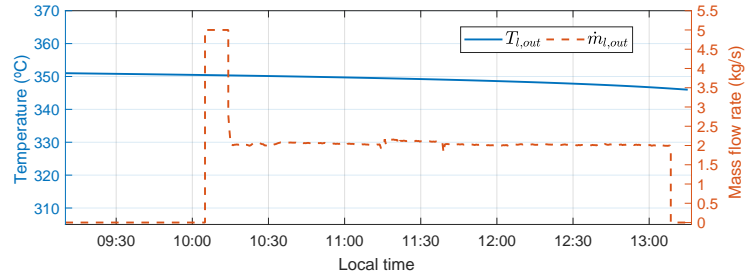


Figure 13: Discharging process: inlet molten salt mass flow rate and temperature

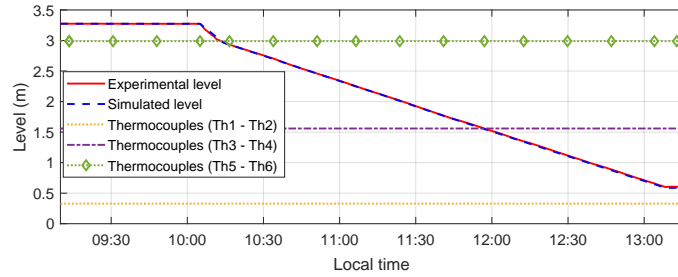


Figure 14: Discharging process: experimental and simulated levels

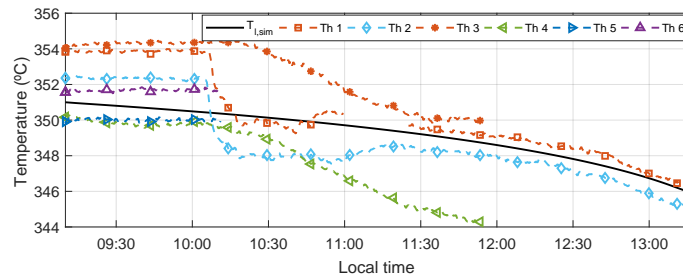


Figure 15: Discharging process: experimental and simulated molten salt temperatures

A flanged thermocouple tree was installed in the tank for this experiment. Several thermocouples at different heights measure molten salt and gas temperatures. The molten salt was heated and then stored in the tank, which was left at rest during 24 h. The initial molten salt level was 3 m, whereas the initial mean molten salt temperature was about 337.4 °C.

A simulation was performed in the same conditions that the experiment in order to validate the model ability to predict thermal losses. The simulation results were compared against experimental data. Fig. 17 shows simulated and

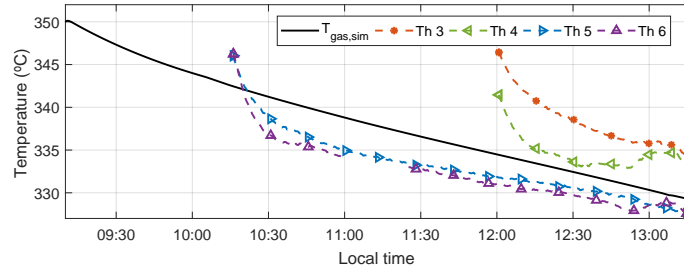


Figure 16: Discharging process: experimental and simulated gas temperatures

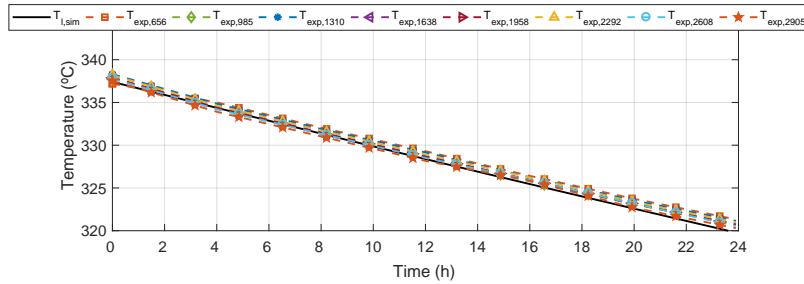


Figure 17: Thermal losses: experimental and simulated molten salt temperatures. $T_{exp,x}$ stands for measured experimented temperature at x mm in height with respect to the tank bottom

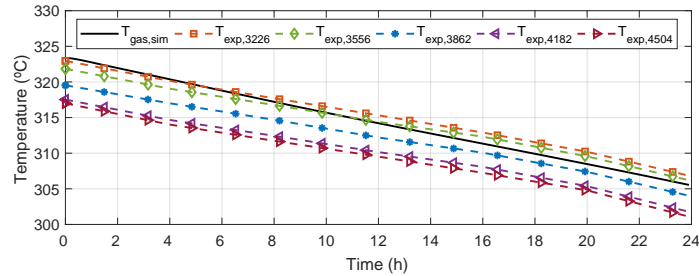


Figure 18: Thermal losses: experimental and simulated gas temperatures. $T_{exp,x}$ stands for measured experimented temperature at x mm in height with respect to the tank bottom

experimental molten salt temperatures during the experiment. Same information but for the gas is shown in Fig. 18. Experimental temperatures, as shown in both pictures' legends, account for the position of the thermocouple with respect to the tank floor in millimeters. It can be seen that there is a good agreement predicting thermal losses. The simulated gas temperature exhibits a

slightly fast dynamic behavior than the real system. Like previous simulations, only a few seconds are required to perform it.

3.3. Thermal Energy Storage (TES) tank simulation tool

With the aim of providing a simulation tool to reproduce the results presented in Sec. 3.2, a simulator of the developed TES tank model was built. This application can be also useful for studying the system dynamics and to evaluate the influence of the model parameters. This simulator is open source and is freely available at <https://ciemat-psa.gitlab.io/surf-simulator/projects/tes-tank-simulator>. Currently, there are binary versions for Linux and Windows platforms.

Figure 19 shows some screenshots of the TES tank simulator. The application includes the Modelica model exported following the FMI standard, input files, experimental results, diagrams and documentation about the model and experiments.

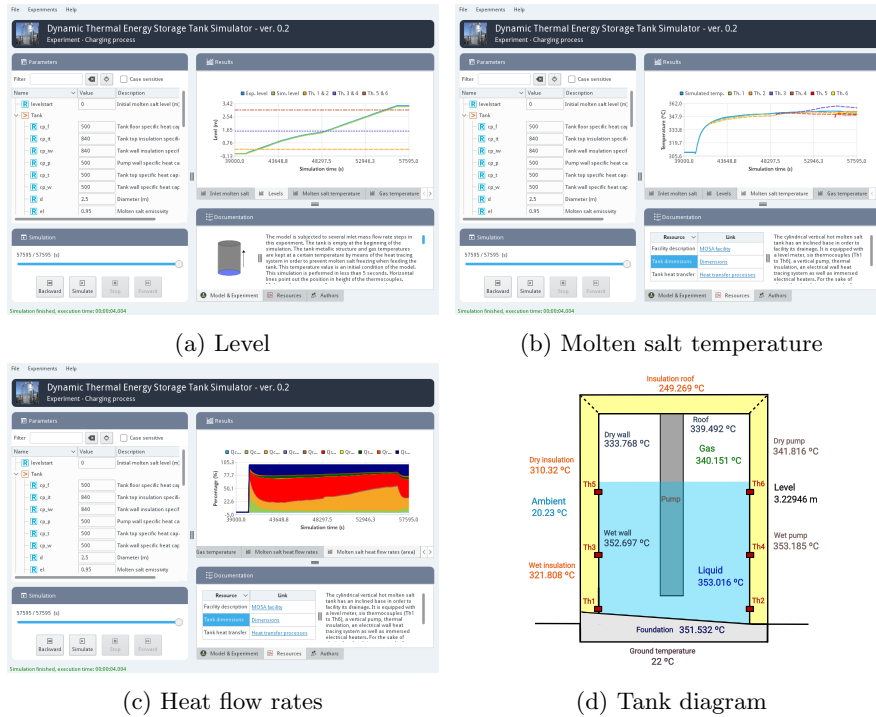


Figure 19: Thermal Energy Storage (TES) tank simulation tool.

In the *experiments* menu, any of the operating days, previously discussed in Sec. 3.2 (charging process, discharging process and thermal losses), can be selected. Model parameters (see Tab. 1) are shown in a tree structure on the top left side, where the user can change their default values. Simulation controls

are shown on the bottom left side. When the simulation is finished, a particular time instant can be selected by manipulating the simulation bar. Inputs and simulation results are shown on the right top side. Several tabs organize this information in plots. For instance, simulated and experimental levels (see Fig. 19a), simulated and experimental molten salt temperatures (see Fig. 19b), simulated heat flow rates (see Fig. 19c). On the bottom right side, there are three tabs, the *authors* tab provides information about the authors, the *resources* tab can include documents, pictures and external links and the *model & experiment* tab provides additional information. There is a thumbnail in this tab. A diagram of the process is displayed in another window when the thumbnail is clicked. This diagram can graphically describe the process and displays information about a particular point in time of the simulation, i.e. tank level, molten salt, gas, insulation and metallic structure temperatures (see Fig. 19d).

Plots have contextual menus which allow the user to change their appearance and configuration. Additionally, results can be exported as data or graphs to files or the clipboard.

4. Conclusions and Future Work

This paper has introduced a dynamic tank model which has been validated against experimental data in three different scenarios: thermal losses estimation at rest, charging and discharging processes. The model properly estimates the liquid level and mean liquid and gas temperatures. All geometrical features, material thermal properties (tank metallic structure, pump, insulation and foundation) and fluids (liquid, gas and ambient) are defined as parameters, therefore they can be changed to adapt the model to different kinds of vertical tanks. The tank model is suitable for dynamic charging and discharging simulations, as well as at predicting thermal losses rates. Simulations are performed fast so the model is suitable for optimization, real-time simulations and model-based control systems.

Future work includes the coupling of the dynamic tank model with the aim of modeling the dynamic behavior of a complete solar thermal power plant. Another task is the analysis, testing and design of charging and discharging control strategies to optimize the plant performance under different meteorological conditions and changes in thermal energy demand.

Acknowledgments

This research has been funded by the Spanish Ministry of Economy, Industry and Competitiveness through ERDF, PLAN E funds (C.N. SolarNOVA ICT-CEPU 2009-02) and the National R+D+i Plan Project DPI2014-56364-C2-1/2-R (ENERPRO-EFFERDESAL).

- [1] Brian M. Adams, Mohamed S. Ebeida, Michael S. Eldred, Gianluca Geraci, John D. Jakeman, Kathryn A. Maupin, Jason A. Monschke, Laura P. Swiler, J. Adam Stephens, Dena M. Vigil, and Timothy M. Wildey. Dakota,

A Multilevel Parallel Object-Oriented Framework for Design Optimization, Parameter Estimation, Uncertainty Quantification, and Sensitivity Analysis: Version 6.5 User's Manual, 2016.

- [2] Azom. Stainless Steel - Grade 321 (UNS S32100).
- [3] Javier Bonilla, Jose A Carballo, Lidia Roca, and Manuel Berenguel. Development of an open source multi-platform software tool for parameter estimation studies in FMI models. In *12th International Modelica conference 2017*, pages 683 – 692, Prague, Czech Republic, 2017.
- [4] Javier Bonilla, Alberto de la Calle, Margarita-Manuela Rodríguez-García, Lidia Roca, and Loreto Valenzuela. Experimental Calibration of Heat Transfer and Thermal Losses in a Shell-and-Tube Heat Exchanger. In *Proc. 11th International Modelica Conference*, pages 873–882, Versailles, France, 2015.
- [5] Javier Bonilla, Margarita M. Rodríguez-García, Lidia Roca, and Loreto Valenzuela. Object-oriented modeling of a multi-pass shell-and-tube heat exchanger and its application to performance evaluation. *IFAC-PapersOnLine*, 28(11):97–102, 2015.
- [6] F. Casella, M. Otter, K. Proelss, C. Richter, and H. Tummescheit. The Modelica Fluid and Media library for modeling of incompressible and compressible thermo-fluid pipe networks. In *Proc. 5th International Modelica Conference*, pages 631–640, Vienna, Austria, 2006.
- [7] Tuncer Cebeci, J. Qasim, and T. Y. Na. Free convective heat transfer from slender cylinders subject to uniform wall heat flux. *Letters in Heat and Mass Transfer*, 1(2):159–162, 1974.
- [8] Y. A. Çengel and A. J. Ghajar. *Heat and Mass Transfer, Fundamentals & Applications (5th edition)*. McGraw-Hill series in mechanical engineering. McGraw-Hill, 2014.
- [9] Daniele Cocco and Fabio Serra. Performance comparison of two-tank direct and thermocline thermal energy storage systems for 1MWe class concentrating solar power plants. *Energy*, 81:526–536, 2015.
- [10] Dassault Systemes. Dymola 2017 FD01 - Multi-Engineering Modeling and Simulation, 2016.
- [11] Fabrizio De Luca, Vittorio Ferraro, and Valerio Marinelli. On the performance of CSP oil-cooled plants, with and without heat storage in tanks of molten salts. *Energy*, 83:230–239, 2015.
- [12] R. Ferri, A. Cammi, and D. Mazzei. Molten salt mixture properties in RELAP5 code for thermodynamic solar applications. *International Journal of Thermal Sciences*, 47(12):1676–1687, dec 2008.

- [13] Georgios Florides and Soteris Kalogirou. Measurements of Ground Temperature at Various Depths. *8th REHVA World Congress*, (May 2016), 2005.
- [14] International Energy Agency. *Solar Energy Perspectives*. IEA Publications, 2011.
- [15] Sarada Kuravi, Jamie Trahan, D. Yogi Goswami, Muhammad M. Rahman, and Elias K. Stefanakos. Thermal energy storage technologies and systems for concentrating solar power plants. *Progress in Energy and Combustion Science*, 39(4):285 – 319, 2013.
- [16] H. Leuenberger and R.A. Person. Compilation of radiation shape factors for cylindrical assemblies. *Asme*, pages 56–A–144, 1956.
- [17] Xiaolei Li, Ershu Xu, Shuang Song, Xiangyan Wang, and Guofeng Yuan. Dynamic simulation of two-tank indirect thermal energy storage system with molten salt. *Renewable Energy*, 2017.
- [18] Y. F. Liu, Z. L. Hu, D. H. Shi, and K. Yu. Experimental investigation of emissivity of steel. *International Journal of Thermophysics*, 34(3):496–506, 2013.
- [19] Isabel Llorente García, José Luis Álvarez, and Daniel Blanco. Performance model for parabolic trough solar thermal power plants with thermal storage: Comparison to operating plant data. *Solar Energy*, 85(10):2443–2460, 2011.
- [20] Flavio Manenti and Zohreh Ravaghi-Ardebili. Dynamic simulation of concentrating solar power plant and two-tanks direct thermal energy storage. *Energy*, 55:89–97, 2013.
- [21] Flavio Manenti and Zohreh Ravaghi-Ardebili. Dynamic simulation of concentrating solar power plant and two-tanks direct thermal energy storage. *Energy*, 55:89–97, 2013.
- [22] Bonnie J. McBride, Michael J Zehe, and Sanford Gordon. NASA Glenn Coefficients for Calculating Thermodynamic Properties of Individual Species. page 297, 2002.
- [23] Rogelio Menéndez, Juan Martínez, Miguel Prieto, Lourdes Barcia, and Juan Sánchez. A Novel Modeling of Molten-Salt Heat Storage Systems in Thermal Solar Power Plants. *Energies*, 7(10):6721–6740, 2014.
- [24] Modelica Association. Modelica Standard Library 3.2.1, 2013.
- [25] Modelica Association. Functional Mock-up Interface for Model Exchange and Co-Simulation, Version 2.0, 2014.
- [26] L.R. Petzold. A description of DASSL: a Differential/Algebraic System Solver. *Scientific Computing*, pages 65–68, 1983.

- [27] Czeslaw O Popiel. Free Convection Heat Transfer from Vertical Slender Cylinders: A Review. *Heat Transfer Engineering*, 29(6):521–536, 2008.
- [28] Kody M. Powell and Thomas F. Edgar. Modeling and control of a solar thermal power plant with thermal energy storage. *Chemical Engineering Science*, 71(2012):138–145, 2012.
- [29] S. N. Rea. Rapid method for determining concentric cylinder radiation view factors. *AIAA Journal*, 13(8):1122–1123, 1975.
- [30] Lidia Roca, Javier Bonilla, Margarita-Manuela Rodríguez-García, Patricia Palenzuela, Alberto de la Calle, and Loreto Valenzuela. Control strategies in a thermal oil - Molten salt heat exchanger. *AIP Conference Proceedings*, 1734:130017–1–130017–8, 2016.
- [31] Rockwool. ProRox WM 960 - Productsheet - Industrial and Tecnical, 2014.
- [32] I. Rodríguez, C.D. Pérez-Segarra, O. Lehmkuhl, and A. Oliva. Modular object-oriented methodology for the resolution of molten salt storage tanks for CSP plants. *Applied Energy*, 109(2013):402–414, 2013.
- [33] M.-M. Rodríguez-García. First Experimental Results of a PTC Facility Using Gas as the Heat Transfer Fluid. In *15th SolarPACES Conference*, Berlin, Germany, 2009.
- [34] Margarita-Manuela Rodríguez-García, Miguel Herrador-Moreno, and Eduardo Zarza. Lessons learnt during the design, construction and start-up phase of a molten salt testing facility. *Applied Thermal Engineering*, 62(2):520–528, jan 2014.
- [35] M. Romero-Alvarez and E. Zarza. Concentrating Solar Thermal Power. In *Handbook of Energy Efficiency And Renewable Energy*, chapter 21, pages 1–98. CRC Press, 2007.
- [36] Piyush Sabharwall, Matt Ebner, Manohar Sohal, Phil Sharpe, Mark Anderson, Kumar Sridharan, James Ambrosek, Luke Olson, and Paul Brooks. Molten salts for high temperature reactors: University of Wisconsin molten salt corrosion and flow loop experiments – Issues identified and path forward. (March):33, 2010.
- [37] H.J. van Antwerpen and G.P. Greyvenstein. Evaluation of a detailed radiation heat transfer model in a high temperature reactor systems simulation model. *Nuclear Engineering and Design*, 238(11):2985–2994, 2008.
- [38] VDI. *VDI Heat Atlas*. Springer, 8st edition, 2010.
- [39] WeGo Systembaustoffe. RockWool ProRox 960 - Technical specification, 2017.

- [40] Edmund Widl, Wolfgang Muller, Atiyah Elsheikh, Matthias Hortenhuber, and Peter Palensky. The FMI++ library: A high-level utility package for FMI for model exchange. *Workshop on Modeling and Simulation of Cyber-Physical Energy Systems, MSCPES 2013* , 2013.
- [41] Fritz Zaversky, Javier García-Barberena, Marcelino Sánchez, and David Astrain. Transient molten salt two-tank thermal storage modeling for CSP performance simulations. *Solar Energy*, 93:294–311, jul 2013.
- [42] Fritz Zaversky, Javier Pérez de Zabalza Asiain, and Marcelino Sánchez. Transient response simulation of a passive sensible heat storage system and the comparison to a conventional active indirect two-tank unit. *Energy*, 139:782–797, 2017.
- [43] A. B. Zavoico. Solar Power Tower - Design Basis Document. Technical Report SAND2001-2100, Sandia National Laboratories, Albuquerque, USA, 2001.